

# EARLY CAREER SCHOLARS IN MATERIALS SCIENCE 2018: INVITED FEATURE PAPER

## Solute stabilization of nanocrystalline tungsten against abnormal grain growth

Olivia K. Donaldson

*Department of Materials Science and Engineering, Stony Brook University, Stony Brook, New York 11794, USA*

Khalid Hattar

*Department of Radiation Solid Interactions, Sandia National Laboratories, Albuquerque, New Mexico 87185, USA*

Tyler Kaub and Gregory B. Thompson

*Department of Metallurgical and Materials Engineering, University of Alabama, Tuscaloosa, Alabama 35487, USA*

Jason R. Trelewicz<sup>a)</sup>

*Department of Materials Science and Engineering, Stony Brook University, Stony Brook, New York 11794, USA*

(Received 5 May 2017; accepted 30 June 2017)

Microstructure and phase evolution in magnetron sputtered nanocrystalline tungsten and tungsten alloy thin films are explored through in situ TEM annealing experiments at temperatures up to 1000 °C. Grain growth in unalloyed nanocrystalline tungsten transpires through a discontinuous process at temperatures up to 550 °C, which is coupled to an allotropic phase transformation of metastable  $\beta$ -tungsten with the A-15 cubic structure to stable body centered cubic (BCC)  $\alpha$ -tungsten. Complete transformation to the BCC  $\alpha$ -phase is accompanied by the convergence to a unimodal nanocrystalline structure at 650 °C, signaling a transition to continuous grain growth. Alloy films synthesized with compositions of W–20 at.% Ti and W–15 at.% Cr exhibit only the BCC  $\alpha$ -phase in the as-deposited state, which indicate the addition of solute stabilizes the films against the formation of metastable  $\beta$ -tungsten. Thermal stability of the alloy films is significantly improved over their unalloyed counterpart up to 1000 °C, and grain coarsening occurs solely through a continuous growth process. The contrasting thermal stability between W–Ti and W–Cr is attributed to different grain boundary segregation states, thus demonstrating the critical role of grain boundary chemistry in the design of solute-stabilized nanocrystalline alloys.



Jason R. Trelewicz

Dr. Jason Trelewicz is an Assistant Professor of Materials Science and Engineering, Director of the Engineered Metallic Nanostructures Laboratory, a Faculty Member of the Institute for Advanced Computational Science, and Director of the NYSTAR-funded High Performance Computing Consortium at Stony Brook University. Professor Trelewicz received his Ph.D. in Materials Science and Engineering from the Massachusetts Institute of Technology in 2008. Prior to joining Stony Brook University in 2012, he spent four years as Research Director at MesoScribe Technologies, Inc. responsible for managing technology development and transition with a focus on harsh environment sensors produced by additive manufacturing processes. Professor Trelewicz's research is on the science of interface engineered alloys with particular emphasis on high-strength and radiation-tolerant nanomaterials for extreme environment applications. His group couples in situ and analytical characterization tools with large-scale atomistic simulations to explore the thermal stability, mechanical behavior, and radiation tolerance of solute-stabilized nanocrystalline alloys, crystalline-amorphous nanolaminates, metallic glass matrix composites, and other unique hierarchical metallic structures. Professor Trelewicz is a recipient of the 2017 DOE Early Career Award for "Enhancing the Performance of Plasma-facing Materials Through Solute-stabilized Nanostructured Tungsten Alloys" and the 2016 NSF Faculty Early Career Development (CAREER) Award for "Interface Engineered Amorphous Alloys for Thermoplastic Forming of Ductile Bulk Metallic Glasses". He also received the 2015 TMS Young Leader Professional Development Award and was selected as a TMS representative for the 2014 Emerging Leaders Alliance Conference. Professor Trelewicz is an active member of the Materials Research Society (MRS), The Minerals, Metals, and Materials Society (TMS), and ASM International.

Contributing Editor: Jürgen Eckert

<sup>a)</sup>Address all correspondence to this author.

e-mail: jason.trelewicz@stonybrook.edu

DOI: 10.1557/jmr.2017.296

## I. INTRODUCTION

The abundance of environments that require advanced materials resistant to high temperature, extreme stresses, and other demanding operating conditions has grown rapidly over the past two decades.<sup>1,2</sup> One particular example to that end is the development of fusion as a clean, sustainable energy source, which relies extensively on tungsten for the design of plasma facing components due to its high melting point, good thermal conductivity, high temperature strength, sputtering resistance, and chemical compatibility with tritium.<sup>3</sup> A number of strategies focused on alloy design have been pursued for enhancing the performance of tungsten for extreme environment applications.<sup>4</sup> Refining of the grain size to the ultrafine and nanocrystalline regimes, in particular, has demonstrated promising results for collectively enhancing the mechanical performance<sup>5,6</sup> and defect accommodation under ion irradiation.<sup>7,8</sup> Unfortunately, the far-from-equilibrium state occupied by nominally pure nanocrystalline metals renders them thermally unstable,<sup>9</sup> and nanostructured tungsten suffers from the same limitation at elevated temperatures.<sup>10</sup>

Thermal instabilities in nanocrystalline metals derive from the energetic penalty associated with the introduction of a high volume fraction of grain boundaries,<sup>11</sup> which promotes grain growth at low homologous temperatures to reduce the total grain boundary area and in turn the system free energy.<sup>12,13</sup> A classic example of this phenomenon is found in nanocrystalline Ni where grain size increased by  $20\times$  at only 30% of its melting point.<sup>14</sup> Similar behavior has been observed across a range of single-component nanocrystalline metals such as cobalt,<sup>15</sup> iron,<sup>16</sup> copper,<sup>17</sup> and silver<sup>18</sup> where microstructural evolution often prescribes to curvature-driven grain growth with the grain boundary velocity,  $v$ , proportional to the local mean curvature of the boundary,  $\kappa$ :

$$v = M_{\text{gb}} \times \gamma_{\text{gb}} \times \kappa \quad (1)$$

In Eq. (1),  $M_{\text{gb}}$  is the grain boundary mobility and  $\gamma_{\text{gb}}$  the grain boundary energy,<sup>19</sup> which capture the kinetic and thermodynamic components of grain growth, respectively. Grain growth in single-component nanocrystalline metals has been modeled using Eq. (1) and demonstrated that an enhanced grain boundary mobility is accompanied by a reduced activation energy for grain growth.<sup>13,17,20</sup> However, the onset of microstructural evolution in a range of nanocrystalline metals often transpires through an abnormal growth process, which has been observed in copper,<sup>21,22</sup> nickel,<sup>21,23</sup> iron,<sup>24</sup> palladium,<sup>13</sup> and cobalt<sup>15</sup> as well as a number of binary nanocrystalline alloys.<sup>25–27</sup> As the average grain size increases from the nanocrystalline to the ultrafine grain regime, abnormal grain growth widely succumbs to curvature-driven mechanisms,<sup>28</sup> thus underscoring the importance of stabilizing the

nanostructure collectively against the initial and late stages of grain growth in nanocrystalline metals.

Abnormal grain growth has been attributed to a number of factors such as nonuniform grain boundary mobility,<sup>29</sup> second-phase particles inhibiting grain boundary migration,<sup>30</sup> and surface energy anisotropy in thin films.<sup>31</sup> In the absence of second-phase particles, the onset of abnormal grain growth follows the mean field theory of Rollett and Mullins<sup>32</sup> and derives from nonuniform grain boundary mobility relating to the interplay between grain boundary properties and local network effects from the surrounding grain structure.<sup>33</sup> Local pinning of the grain boundaries also augments their mobility due to a number of factors such as grain boundary faceting,<sup>34,35</sup> surface energy-driven thermal grooving in thin films,<sup>36</sup> and the presence of second-phase particles in alloys.<sup>30</sup> The latter has been explored in nanocrystalline Cu–Ta<sup>37</sup> and Au–Pt<sup>38</sup> systems, which exhibited solute-rich nanoprecipitates that inhibit grain boundary migration at temperatures exceeding 50% of the respective melting points for each alloy. Grain boundary solute enrichment also has thermodynamic implications for nanostructure stability where reductions in the interfacial free energy due to grain boundary segregation can suppress or effectively eliminate the driving force for grain growth.<sup>11,39,40</sup> The propensity for solute to segregate to the grain boundaries in a particular alloy system is captured by the ratio of the enthalpy of segregation to the heat of mixing,<sup>41</sup> which has important implications for the stability of the microstructure.

A direct comparison of solute distribution and thermal stability was accomplished in the nanocrystalline iron system employing Mg and Cu as alloying elements.<sup>42</sup> The Fe–Mg system exhibited stable nanocrystalline grain structures with Mg segregation to the grain boundaries while Fe–Cu exhibited a phase-separated microstructure with limited grain boundary segregation and more extensive grain growth, which aligned with predictions from lattice Monte Carlo modeling. These principles have also been investigated in tungsten alloys with a stability map constructed by Chookajorn et al.<sup>10</sup> from which Ti was identified as a potential candidate for producing a nanocrystalline-stable material. An alloy of W–20 at.% Ti synthesized via high energy ball milling exhibited an as-milled grain size of approximately 20 nm that remained stable at 1100 °C for one week<sup>43</sup>; unalloyed nanocrystalline tungsten coarsened by over an order of magnitude to a grain size of  $>0.5 \mu\text{m}$  under identical conditions. Similar behavior has been observed in a range of other alloy systems including W–Cr<sup>44</sup> and Hf–Ti<sup>45</sup> as well as in nanocrystalline ceramic materials such as La-doped yttria-stabilized zirconia (YSZ).<sup>46</sup>

In this study, thermal stability of magnetron sputtered nanocrystalline tungsten and tungsten alloy thin films is explored through in situ transmission electron microscopy (TEM) annealing experiments up to 1000 °C. Abnormal grain growth and its transition to a continuous,

curvature-driven growth process in unalloyed nanocrystalline tungsten are first characterized by tracking the evolution of select grains as a function of annealing temperature in bright-field TEM images. Insights into the mechanisms facilitating discontinuous grain growth are then provided by considering the interplay between phase transitions, texture, surface energy effects, and grain boundary misorientation distributions. To combat microstructural instabilities that lead to the early onset of grain coarsening, solute additions are investigated in the W–Ti and W–Cr binary alloy systems. Grain size distributions following heat treatment at 1000 °C are compared to understand the implications of alloy selection for thermal stability, and finally discussed in the context of the underlying solute distributions quantified through scanning transmission electron microscopy (STEM) and electron energy loss spectroscopy (EELS) measurements.

## II. MATERIALS AND METHODS

Magnetron sputtered W, W–20 at.% Ti, and W–15 at.% Cr thin films were deposited in an AJA ATC-1500 stainless-steel chamber from >99.95% pure elemental targets obtained from the Kurt J. Lesker company (Jefferson Hills, Pennsylvania). The films were deposited to a nominal thickness of 20–30 nm on polished NaCl substrates acquired from International Crystal Laboratories (#0002A-4549; Garfield, New Jersey). Prior to deposition, the substrates were heated to 150 °C for 1 h to remove surface water. The sputtering chamber was evacuated to  $<6.66 \times 10^{-6}$  Pa before flowing in ultrahigh purity argon to a pressure of 0.266 Pa at a rate of 10 standard cubic centimeters per minute. Films were deposited at 100 °C and subsequently cooled to ambient temperature prior to removal from the chamber. Deposition rates, measured from the total film thickness via small angle X-ray reflectivity<sup>47</sup> using an X'Pert Philips X-ray diffractometer (Philips, Almelo, the Netherlands) operated with a Cu K $\alpha$  source at 45 kV and 40 mA, ranged from 0.12 to 0.18 nm/s depending on composition.

In situ annealing of the unalloyed nanocrystalline tungsten films used a Hummingbird ETEM 1500 series heating holder (Hummingbird Scientific, Lacey, Washington) in a JEOL JEM 2100 TEM (JEOL Ltd., Tokyo, Japan). Films were heated at a rate of 5 °C/min to 300, 450, 550, and 650 °C where they were held for 5–10 min before being cooled to room temperature over a 1 h period. Precession electron diffraction (PED) was conducted on the annealed films using the NanoMEGAS ASTAR mapping system (NanoMEGAS SPRL, Brussels, Belgium). All scans underwent an ambiguity and noise reduction, which included the removal of anomalous spikes and a zero-solution extrapolation. In situ annealing of the nanocrystalline tungsten alloy films was conducted up to 1000 °C using a Gatan heating holder (Model #628;

Gatan, Inc., Pleasanton, California) in a Philips CM30 TEM (Philips, Hillsboro, Oregon) operated at 300 kV. The temperature was manually ramped to 1000 °C where upon the films were held for 20 min prior to cooling over a 1 h period. Images and videos of these films were acquired by the TVIPS (TVIPS GmbH, Gauting, Germany) and Gatan Digital Micrograph software (Gatan Inc., Pleasanton, California), respectively. Image and video analysis was performed using ImageJ (U.S. National Institute of Health, Bethesda, Maryland), Adobe Photoshop, and Adobe Premier (Adobe Systems, San Jose, California) with grain orientation maps produced via the Oxford Tango software package (Oxford Instruments, Abingdon, England).

Phase analysis was conducted by generating radial intensity plots from the selected area electron diffraction patterns where the intensity was integrated over all azimuthal angles as a function of distance from the center of the direct beam, which was converted to Bragg angles using a wave length of 0.0273 Å.<sup>48</sup> Phase indexing used the method described by Edington<sup>49</sup> that compares the ring spacing ratios to the reciprocal of the known ratio of d-spacings for all possible crystal structures of interest. Solute distributions in the alloys were characterized using a Hitachi HD2700C STEM (Hitachi, Ltd., Tokyo, Japan) equipped with a Gatan high-resolution Enfina detector (Gatan Inc., Pleasanton, California) at the Center for Functional Nanomaterials at Brookhaven National Laboratory. High angle annular dark field (HAADF) imaging in conjunction with EELS were used to map Ti and Cr solute additions based on their known electron binding energies<sup>50</sup> of 455 and 574 eV, respectively, relative to 1809 eV for W. EELS was selected for its enhanced resolution of small features, which is ideal for correlating elemental segregation to grain boundaries in the TEM.<sup>51</sup>

## III. MICROSTRUCTURAL EVOLUTION IN NANOCRYSTALLINE TUNGSTEN THIN FILMS

In this section, microstructural evolution in sputter-deposited nanocrystalline tungsten thin films is described at temperatures up to 650 °C. In situ approaches enabled real-time imaging of the nanostructure through annealing, which was complemented with post-mortem PED and grain tracking analyses to uncover transitions in the growth mechanisms as a function of temperature. The as-deposited tungsten film exhibited a nanocrystalline grain structure as evident in the bright-field image in Fig. 1(a), and from the corresponding grain size distribution in Fig. 1(b), the mean grain size of the as-deposited film was  $10 \pm 3$  nm. The electron diffraction pattern contained a large number of distinct spots indicative of a nanocrystalline state. Indexing of this diffraction pattern produced the normalized integrated radial intensity profile in Fig. 1(c), which revealed a two-phase structure containing metastable  $\beta$ -tungsten with the

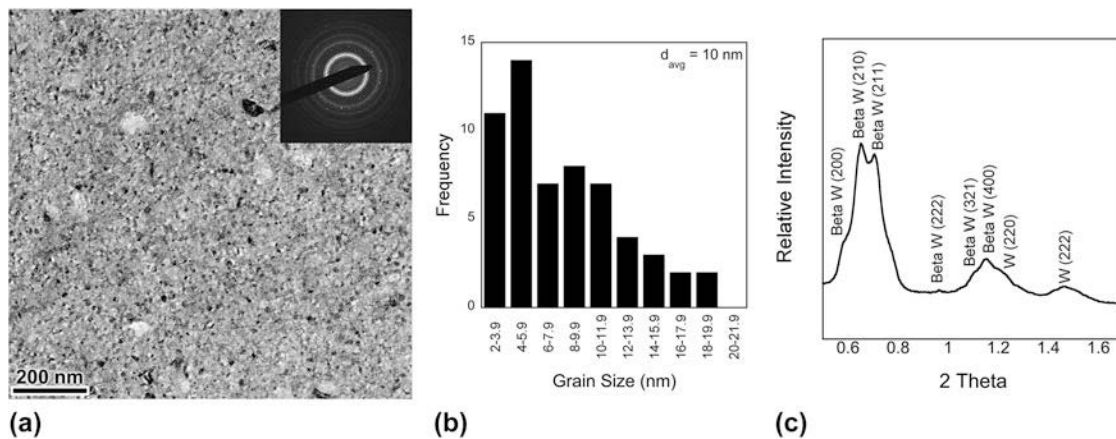


FIG. 1. (a) Bright-field TEM image of the as-deposited nanocrystalline tungsten film with the selected area diffraction pattern shown in the inset, (b) corresponding grain size distribution with a mean grain size of approximately 10 nm, and (c) integrated radial intensity profile determined from the inset in (a) revealing a two-phase structure composed primarily of metastable  $\beta$ -tungsten and BCC  $\alpha$ -tungsten appearing at higher Bragg angles.

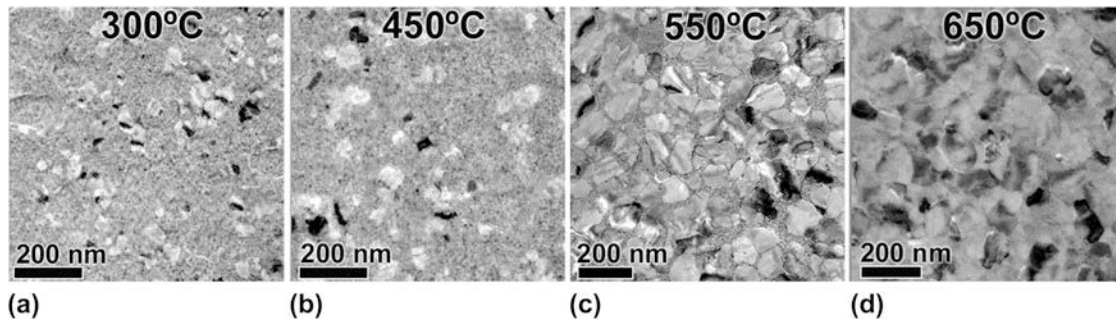


FIG. 2. Bright-field images of the nanocrystalline tungsten films at (a) 300 °C, (b) 450 °C, (c) 550 °C and (d) 650 °C. The as-deposited unimodal nanocrystalline structure evolved to a bimodal distribution of grain sizes at the intermediate annealing temperatures, ultimately converging back to a unimodal grain structure at 650 °C.

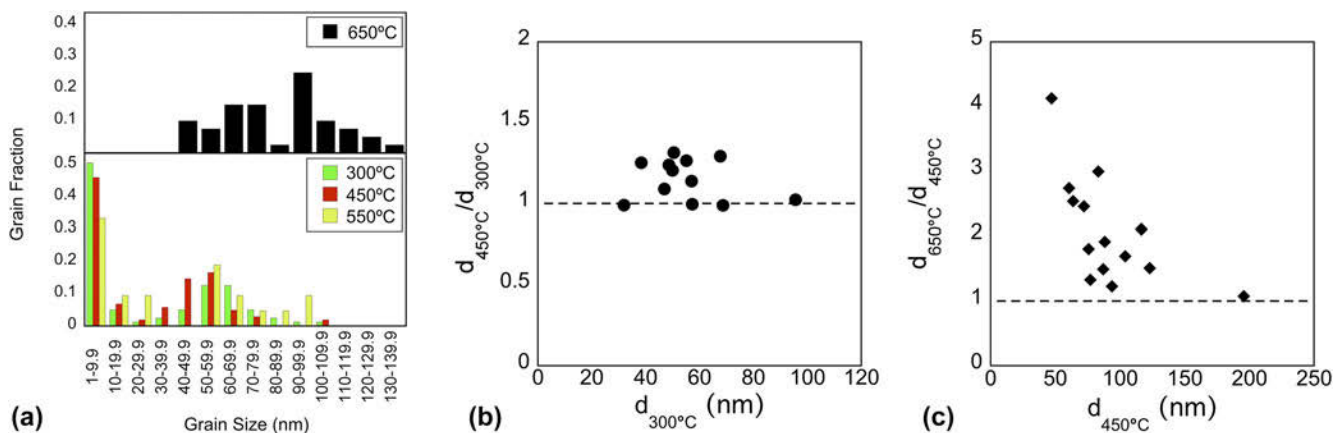


FIG. 3. (a) Grain size distributions for the annealed tungsten films delineated for the bimodal grain size distributions at intermediate annealing temperatures and unimodal nanocrystalline structure at 650 °C. Normalized grain size as a function of the initial grain size for the tracking of individual grains over the temperature ranges of (b) 300–450 °C and (c) 450–650 °C. The size of the outlined grains remained consistent for the temperature range in (b) whereas curvature-driven grain growth transpired over the higher temperature range in (c).

A-15 cubic structure<sup>52</sup> mixed with BCC  $\alpha$ -tungsten. The  $\alpha$ -phase was primarily detected through the appearance of reflections at high Bragg angles; however, other peaks are likely present at low diffraction angles but not evident due to the overlap with the higher intensity  $\beta$ -tungsten

reflections. The presence of the metastable  $\beta$ -phase is common in tungsten thin films deposited via magnetron sputtering,<sup>53</sup> and its implications for microstructural evolution and thermal stability are explored in the remainder of this section.

Initial coarsening of the nanostructure transpired through a discontinuous growth process where a subset of grains grew heterogeneously at 300 °C as evident in the bright-field image shown in Fig. 2(a). The resulting bimodal grain structure, evident in the grain size histogram of Fig. 3(a), contained a distribution of large nanocrystalline grains embedded within the nanocrystalline matrix retained from the as-deposited state with a mean grain size of  $30 \pm 30$  nm; this large standard deviation was attributed to the bimodal distribution of grain sizes. As shown in Fig. 2(b), a similar grain structure was observed upon heating to 450 °C, and changes were not qualitatively discernible in the size or distribution of the larger nanocrystalline grains. The mean size from the histogram was  $30 \pm 26$  nm, which was consistent with the results at 300 °C. However, the number fraction of larger nanocrystalline grains (i.e., with size greater than 20 nm) increased by 29%, which was attended by a 5% decrease in the relative fraction of smaller grains occupying the initial nanocrystalline matrix. A further increase in the temperature to 550 °C produced a conspicuous increase in the number of larger grains that evolved from the small grained nanocrystalline matrix as evident in Fig. 2(c). This manifested as an increase in the mean grain size to  $48 \pm 33$  nm that was accompanied by an additional 22% increase in the fraction of larger grains and a 19% reduction in the fraction of the smaller nanocrystalline grains from the histogram in Fig. 3(a). The bimodal grain structure eventually succumbed to a unimodal nanocrystalline structure at 650 °C shown in Fig. 2(d) with a mean grain size of approximately  $87 \pm 25$  nm, thus signaling a transition to a continuous grain growth process.

The evolution of individual grains was tracked at temperatures of 300, 450, and 650 °C to confirm the transition from abnormal to continuous grain growth. A subset of larger grains embedded in the as-deposited nanocrystalline matrix was first outlined at 300 °C, and the corresponding grains were mapped in the bright-field

image during heating to 450 °C. The individual sizes of the mapped grains were measured at both temperatures, and the ratio of grain sizes are plotted as a function of the original grain size at 300 °C in Fig. 3(b). The tracked grains exhibited very limited growth over the temperature range of 300–450 °C as evidenced by the grouping of the data points around unity across all initial grain sizes spanning the range of 20–80 nm. Combined with the increase in the number fraction of larger nanocrystalline grains from Fig. 3(a), microstructural evolution was dominated by abnormal grain growth at temperatures up to 450 °C. Results from mapping of individual grains over the second temperature range of 450–650 °C are depicted in Fig. 3(c) normalized and plotted against the initial grain size of each mapped grain at 450 °C. An inverse relationship emerged where smaller nanocrystalline grains exhibited accentuated growth relative to the larger grains spanning the range of 50–200 nm, which is the characteristic of curvature-driven grain growth and substantiates the transition to continuous grain growth in the nanocrystalline tungsten films.

Phase evolution during the abnormal and continuous grain growth regimes was explored through analysis of the selected area electron diffraction patterns corresponding to the bright-field images at temperatures of 300, 550, and 650 °C in Fig. 2, and the resulting normalized integrated radial intensity profiles are depicted in Figs. 4(a)–4(c), respectively. At 300 °C near the onset of abnormal grain growth, the film retained the two-phase structure from the as-deposited state as evidenced by the presence of reflections for both the metastable  $\beta$ -phase and BCC  $\alpha$ -phase. Increasing the temperature to 550 °C produced a significant increase in the intensities of the BCC  $\alpha$ -tungsten peaks in Fig. 4(b) while only a single (321) reflection remained for the  $\beta$ -phase. The emergence of  $\alpha$ -tungsten as the predominant phase in the  $\alpha$ - $\beta$  film was attributed to an allotropic transformation

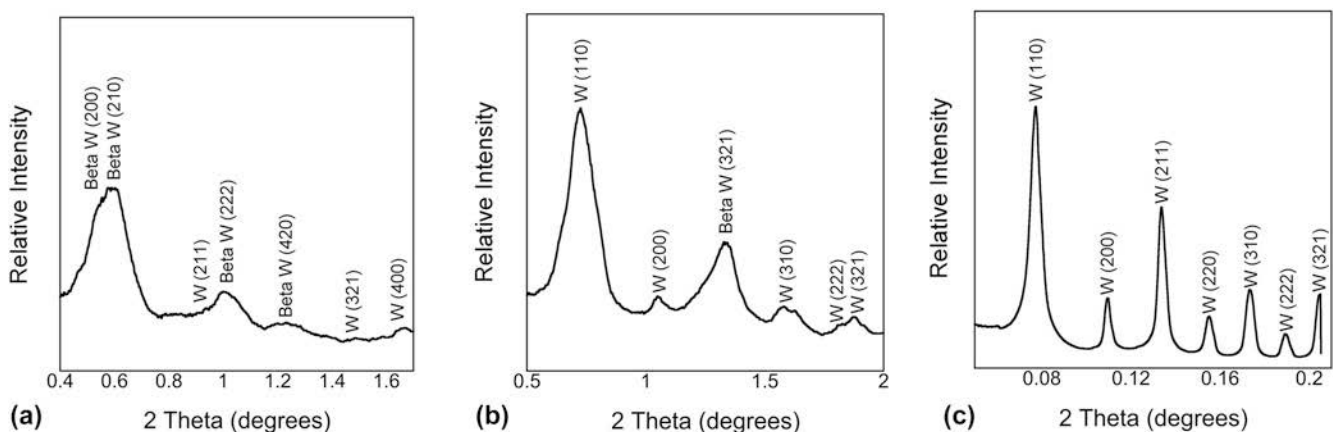


FIG. 4. Integrated radial intensity profiles acquired at temperatures of (a) 300 °C and (b) 550 °C on the bimodal nanocrystalline structures during abnormal grain growth and at (c) 650 °C upon convergence to a unimodal nanocrystalline structure. The  $\alpha$ - $\beta$  two-phase tungsten film evolved to single-phase BCC  $\alpha$ -tungsten through an allotropic phase transformation.

of the metastable  $\beta$ -phase, which aligned with the increase in the number fraction of larger nanocrystalline grains and attendant decrease in the relative fraction of the small nanocrystalline grains from the as-deposited state. The transition to continuous grain growth at 650 °C was accompanied by a complete transformation of the films to BCC  $\alpha$ -tungsten as evidenced by the absence of  $\beta$  reflections in Fig. 4(c). Collectively, these results suggested that the allotropic phase transition was central in contributing to the

formation of bimodal grain size distributions through abnormal grain growth, which ultimately converged to a unimodal grain structure upon completion of this phase transformation process.

The coupling between allotropic phase transformations and microstructural evolution through discontinuous grain growth has been demonstrated in nanocrystalline cobalt where face centered cubic (FCC)  $\alpha$ -Co grains with sizes greater than 100 nm emerged discontinuously in the as-deposited hexagonal

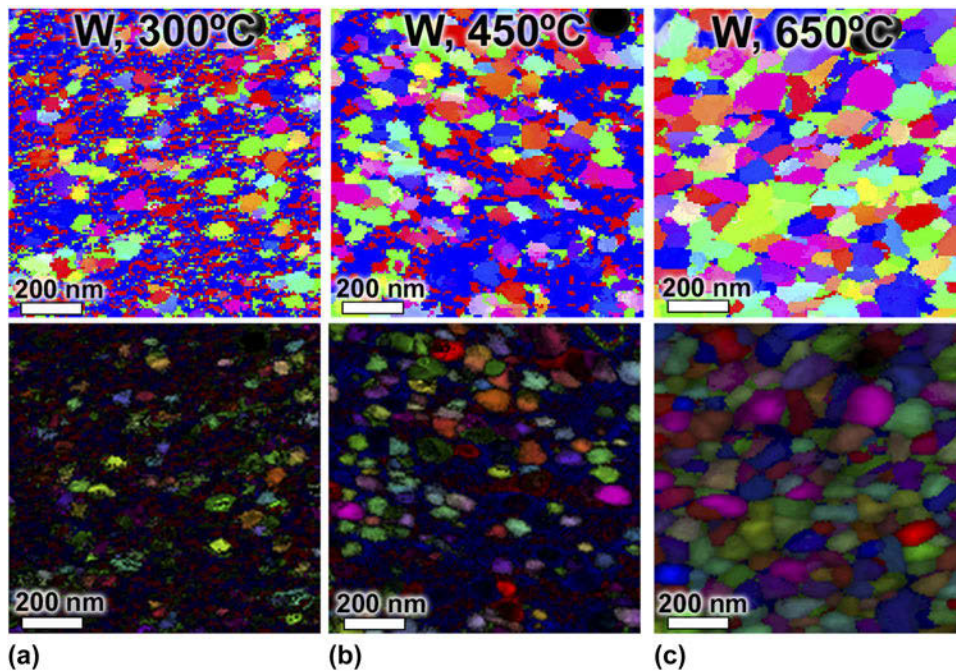


FIG. 5. Precession electron diffraction orientation maps (upper) and combined reliability-orientation maps (lower) at (a) 300 °C, (b) 450 °C, and (c) 650 °C. Grains are colored according to the IPFs in Fig. 6, and the black regions in the reliability-orientation maps capture the low reliability index for grains  $\leq 10$  nm in size within the smaller grain size nanocrystalline matrix. The reader is referred to the web version of this article for interpretation of references to color.

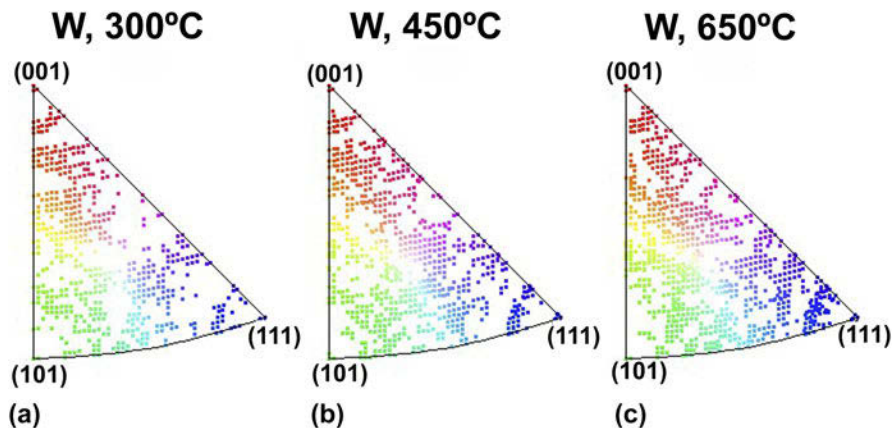


FIG. 6. Inverse pole figures for the combined reliability-orientation maps in Fig. 5 at (a) 300 °C, (b) 450 °C, and (c) 650 °C. Each point corresponds to the orientation of an individual grain and employs an identical coloring scheme. A random polycrystalline texture was apparent across all temperatures indicating that no preferential orientations emerged during the abnormal or continuous growth regimes. The reader is referred to the web version of this article for interpretation of references to color.

close packed (HCP)  $\epsilon$ -Co nanocrystalline matrix with an average grain size of 13 nm.<sup>54</sup> Similarly in the as-deposited nanocrystalline tungsten films composed largely of  $\beta$ -tungsten, a thermodynamic driving force existed for this metastable phase to transform to the equilibrium BCC  $\alpha$ -phase,<sup>52</sup> which was in competition with a large driving force for grain growth. Consequently, phase and microstructural instabilities were inherently coupled in the nanocrystalline tungsten films with the phase transition driving discontinuous grain growth, which is in good agreement with the observations in nanocrystalline cobalt as well as a range of other materials.<sup>25,26,55</sup> We finally note that in cobalt, the addition of 1.1 at.% P shifted the allotropic phase transition and concomitant onset of abnormal grain growth to higher temperatures,<sup>56</sup> thus suggesting that alloying can stabilize nanocrystalline materials against sudden losses in thermal stability due to discontinuous coarsening events.

Film texture has also been demonstrated to augment thermal stability in nanocrystalline nickel thin films by locally constraining grain growth and in turn, producing

bimodal grain size distributions<sup>57</sup> that are similar to the grain structures observed in the nanocrystalline tungsten thin films. To probe the effect of crystallographic orientation through the abnormal and continuous growth regimes, grain orientation and combined reliability-orientation maps were acquired at temperatures of 300, 450, and 650 °C via PED and are depicted in Figs. 5(a)–5(c) colored according to the corresponding inverse pole figures in Figs. 6(a)–6(c). Measurements in the as-deposited nanocrystalline matrix that contained grain sizes  $\leq 10$  nm exhibited low reliability due to the difficulty in resolving orientation for grains sizes in this range via PED.<sup>58</sup> Consequently, only those grains within the reliability threshold during discontinuous grain growth were incorporated into the orientation analysis. The combined reliability-orientation maps exhibited random grain orientations, which was substantiated in Fig. 6 where each point on the inverse pole figures corresponded to an individual grain from the PED maps in Fig. 5. The uniform distribution of grain orientations apparent at each temperature is characteristic of a random polycrystalline texture, and indicates that no preferential

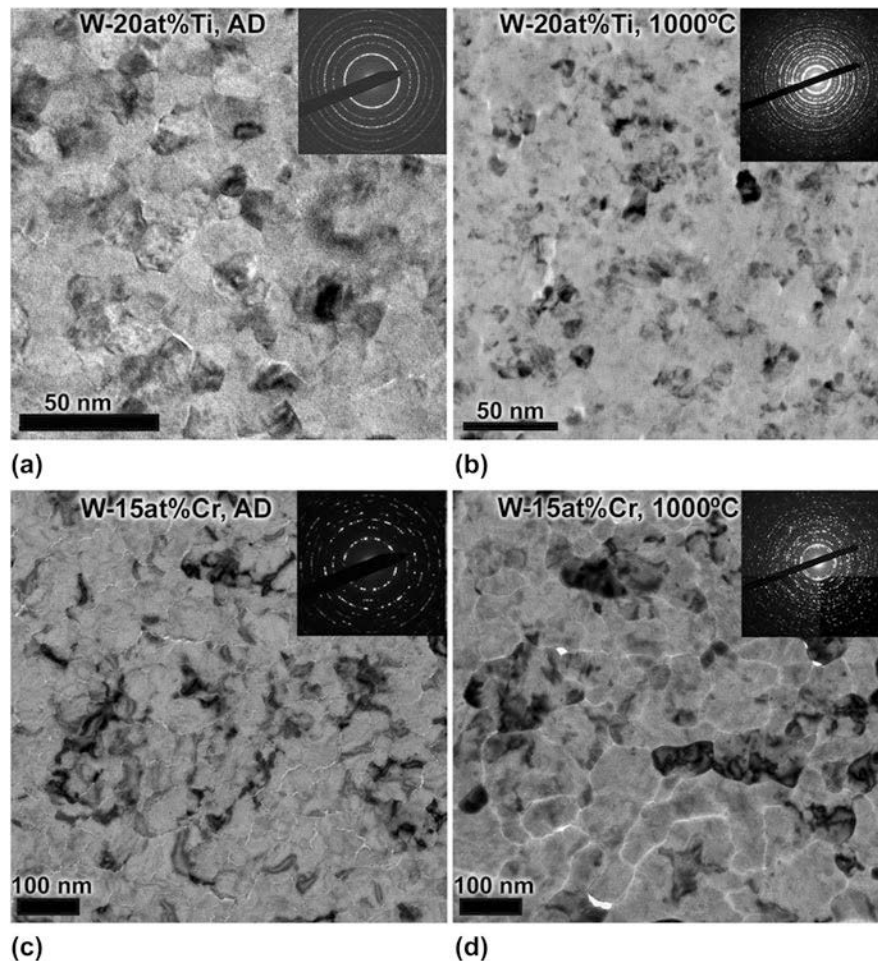


FIG. 7. Bright-field images and selected area diffraction patterns for the nanocrystalline tungsten alloy thin films including (a) as-deposited W-20 at.% Ti, (b) 1000 °C annealed W-20 at.% Ti, (c) as-deposited W-15 at.% Cr, and (d) 1000 °C annealed W-15 at.% Cr.

grain orientations emerged during the abnormal or continuous growth regimes.

Two additional caveats relating to the role of surface energy and nonuniform grain boundary mobility in the onset of abnormal grain growth are finally noted. Surface energy effects in thin films are known to produce thermal grooving at the intersection of grain boundaries with the film surface,<sup>59</sup> which has been connected to local pinning of the boundaries<sup>31,60</sup> and the growth of grains through a discontinuous process.<sup>36</sup> Given that the nanocrystalline tungsten films were appreciably thin (i.e., 25–30 nm), surface energy effects likely contributed to the onset of abnormal grain growth and the rate at which metastable  $\beta$  transformed to the equilibrium  $\alpha$ -phase. Nonuniform grain boundary mobility has been explored in the context of grain boundary energy<sup>61–63</sup> with implications for the formation of anisotropic grain boundary character distributions.<sup>64</sup> In nanocrystalline Ni, abnormal grain growth has been attributed to the preferential migration of high-mobility coincident site lattice (CSL) boundaries.<sup>21</sup> Boundary fractions could not be quantified for the bimodal structures due to the aforementioned reliability issues; however, analysis of the boundary fractions from Fig. 5(c) revealed a uniform distribution of low-energy CSL boundaries in the unimodal grain structure, which is consistent with prior grain growth studies in nanocrystalline metals.<sup>23,65</sup> Surface energy and nonuniform grain boundary mobility effects thus likely complemented the allotropic phase transformation in driving initial microstructural evolution through abnormal grain growth and its transition to continuous, curvature-driven growth upon convergence to a unimodal nanocrystalline structure.

#### IV. SOLUTE STABILIZATION AGAINST ABNORMAL GRAIN GROWTH

Nanocrystalline tungsten thin films exhibited an allotropic phase transformation at low homologous temperatures that was coupled with abnormal grain growth, and the transition to continuous grain growth above 550 °C coincided with complete transformation of the metastable  $\beta$ -phase to the equilibrium BCC phase of tungsten. The effect of solute additions on the as-deposited state of tungsten and stabilization of its nanostructure against abnormal grain growth is described in this section at temperatures up to 1000 °C. Thin films of W–20 at.% Ti and W–15 at.% Cr were sputter deposited using identical deposition procedures to the unalloyed nanocrystalline tungsten films. These particular alloy compositions were selected based on their propensity to produce nanocrystalline stable states as predicted from the regular nanocrystalline solution model,<sup>10</sup> which has been demonstrated in both systems using powder metallurgy

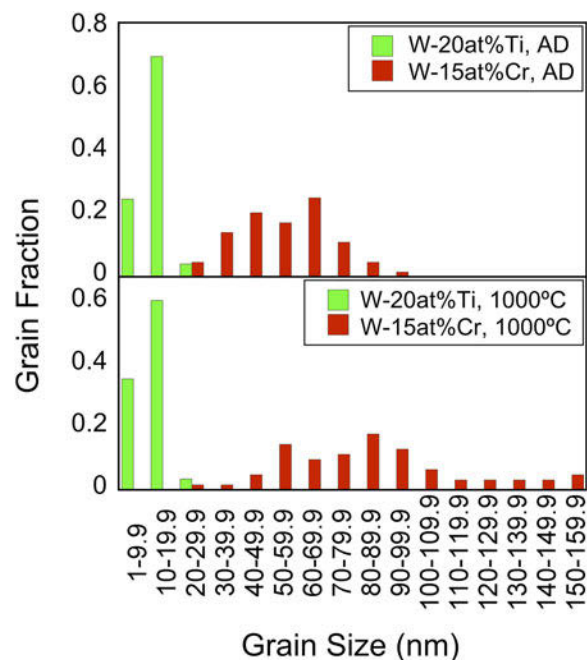


FIG. 8. Grain size distributions for the W–20 at.% Ti and W–15 at.% Cr alloys in the as-deposited state (upper) and following heat treatment at 1000 °C (lower). A shift to larger nanocrystalline grain sizes was apparent in the W–Cr alloy and indicative of grain growth whereas the W–Ti alloy exhibited little change in the overall grain size distribution.

techniques.<sup>43,44</sup> Our analysis focuses on mapping nanostructure stability collectively with solute distributions in as-deposited and heat treated thin film samples using in situ TEM annealing combined with STEM-EELS analysis.

Sputter deposition of W–20 at.% Ti produced the nanocrystalline grain structure shown in Fig. 7(a) with a mean grain size of  $14 \pm 4$  nm from the histogram in Fig. 8 for the as-deposited condition. This structure remained stable through in situ TEM annealing of the film at 1000 °C as evident in Fig. 7(b), and was reflected in the mean grain size exhibiting only a subtle increase to  $18 \pm 4$  nm in the histogram. The W–15 at.% Cr film also exhibited a nanocrystalline grain structure in the as-deposited state as shown in Fig. 7(c), but with a larger initial grain size of  $55 \pm 17$  nm from the histogram in Fig. 8. It was difficult to ascertain qualitative changes to the grain structure in Fig. 7(d) upon annealing of the W–Cr film; however, the mean grain size in the histogram evolved to  $86 \pm 31$  nm, corresponding to a 56% increase from the as-deposited grain size. The grain boundaries in the bright-field image in Fig. 7(d) also appeared brighter relative to the intragranular regions of the film, which was attributed to thickness contrast. The emergence of locally thin regions coinciding with the grain boundaries suggests that annealing promoted the formation of grain boundary voids, gaps, and/or grooving.



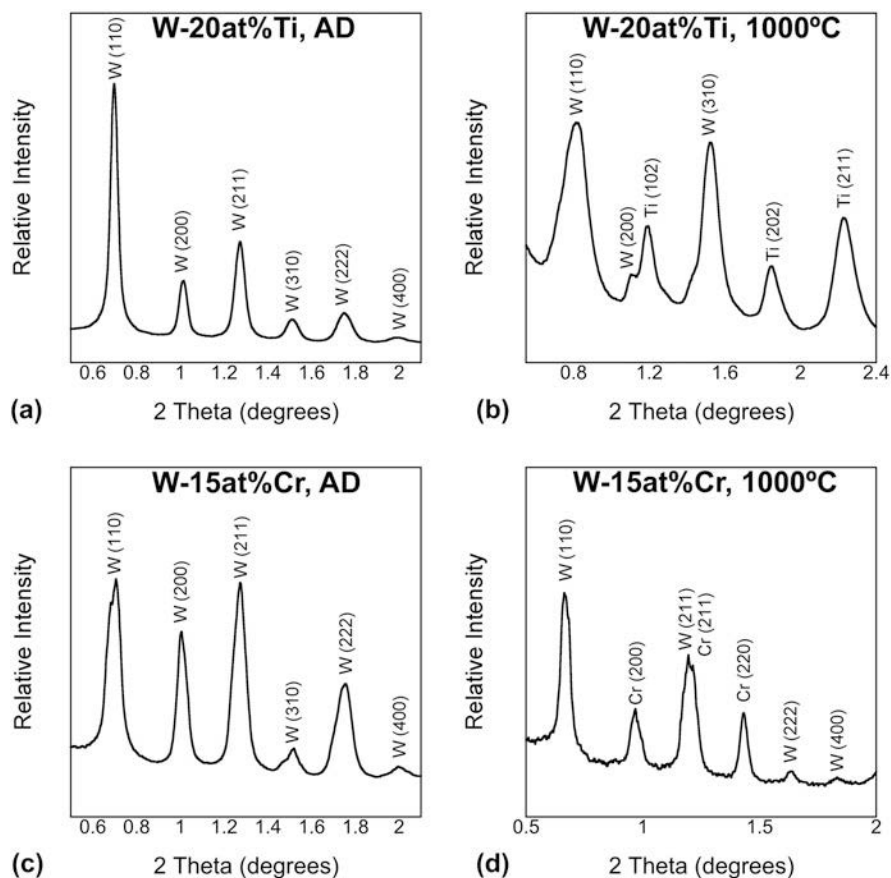


FIG. 9. Integrated radial intensity profiles from the selected area electron diffraction patterns in Fig. 7 for (a) as-deposited W–20 at.% Ti, (b) 1000 °C annealed W–20 at.% Ti, (c) as-deposited W–15 at.% Cr, and (d) 1000 °C annealed W–15 at.% Cr. The emergence of Ti and Cr peaks in (b) and (d), respectively, indicated that solute-rich second-phases formed upon annealing at 1000 °C.

Both alloy films exhibited significantly enhanced thermal stability relative to their unalloyed counterpart, and the addition of alloying elements eliminated abnormal grain growth with microstructural evolution instead transpiring solely through continuous grain growth. In unalloyed tungsten, this transition aligned with transformation of the metastable  $\beta$ -phase to the stable BCC  $\alpha$ -phase of tungsten. A phase analysis was conducted on the alloy films in the as-deposited and annealed conditions, and the integrated radial intensity profiles are shown in Fig. 9. In the as-deposited state, predominant  $\alpha$ -tungsten reflections were evident in both the W–20 at.% Ti and W–15 at.% Cr films in Figs. 9(a) and 9(c), respectively. The addition of alloying elements in solid solution thus eliminated the formation of the metastable  $\beta$ -phase and in turn, stabilized the  $\alpha$ -phase in thin film nanocrystalline tungsten. The appearance of subtle shoulders on the (110) and (310) reflections toward lower Bragg angles of the W–Cr film suggested that some small amount of a Cr-rich phase was present; however, quantitative indexing of these peaks was difficult due to their low intensity and overlap with the  $\alpha$ -tungsten reflections. Annealing of the films produced distinguishable Ti and

Cr peaks in Figs. 9(b) and 9(d), respectively, which indicated that a solute-rich second phase precipitated within the tungsten solid solution during the 1000 °C anneal of both alloy films.

Previous studies on alloys of nominally identical composition produced via high-energy ball milling uncovered the formation of a heterogeneous solute distribution upon annealing with some noteworthy distinctions between W–Ti<sup>43</sup> and W–Cr.<sup>44</sup> In the W–Ti system, Ti-depleted regions were detected following an 1100 °C heat treatment that were comparable to the grain size, suggesting that the Ti atoms were segregated to the grain boundaries. Conversely, Cr-rich nanoscale precipitates were identified predominantly at the grain boundaries upon annealing at 950 °C, and an increase in temperature to 1400 °C produced a duplex nanostructure containing both Cr-rich grains and Cr segregation to the grain boundaries. Our data provides an opportunity to understand the implications of heterogeneous solute distributions for the grain size stability as the deposition and annealing conditions were identical for both alloy compositions.

STEM measurements were used to map the distribution of the solute-rich phases in the alloy films leveraging

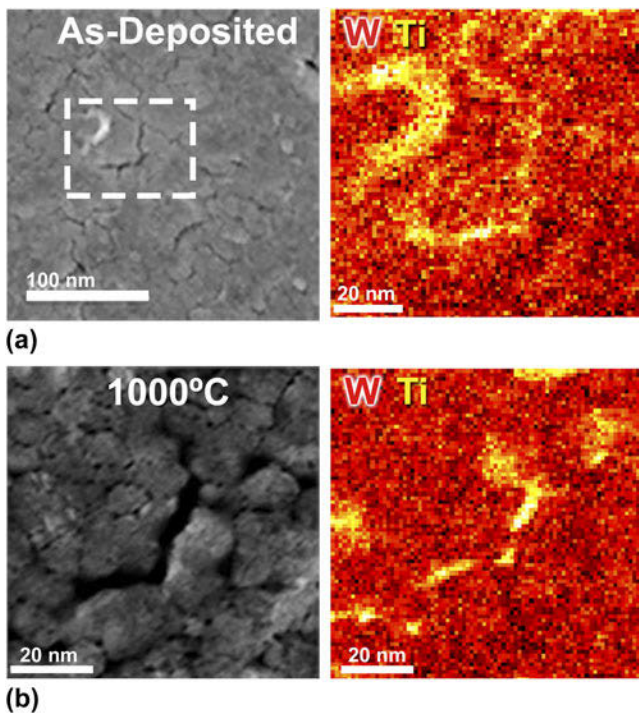


FIG. 10. HAADF images and EELS maps for the W-20 at.% Ti film in the (a) as-deposited and (b) 1000 °C annealed conditions. The EELS maps correspond to the outlined region in the HAADF image in (a) and from the entire image in (b). The as-deposited films exhibited subtle grain boundary segregation, which became more pronounced following heat treatment.

HAADF imaging collectively with EELS analysis to correlate solute distributions with underlying microstructural features. The HAADF image of the as-deposited W-Ti film is shown in Fig. 10(a) with the corresponding elemental map produced from the EELS scan also depicted. The Z-contrast in the HAADF image indicates that compositional inhomogeneities were present in the as-deposited W-Ti film, which was confirmed in the EELS map from the selected region of the HAADF image. Annealing of the W-Ti film amplified this solute partitioning as evidenced in Fig. 10(b). The spatial distribution of Ti in the as-deposited and annealed films was commensurate with the grain size, thus suggesting Ti segregation to the grain boundaries. A heterogeneous solute distribution was also detected in the as-deposited W-Cr film in Fig. 11(a); however, it was difficult to ascertain whether the Cr-rich regions aligned with the grain boundary network. A noticeable change in the solute distribution was uncovered upon annealing of the W-Cr film at 1000 °C. The EELS map in Fig. 11(b) demonstrated extended Cr-rich regions that coincided with the finest grain sizes in the tail of the distributions of the annealed film in Fig. 8, i.e., for grain sizes <40 nm. The appearance of Cr-rich grains also aligned with the emergence of conspicuous Cr reflections in the selected area electron diffraction pattern.

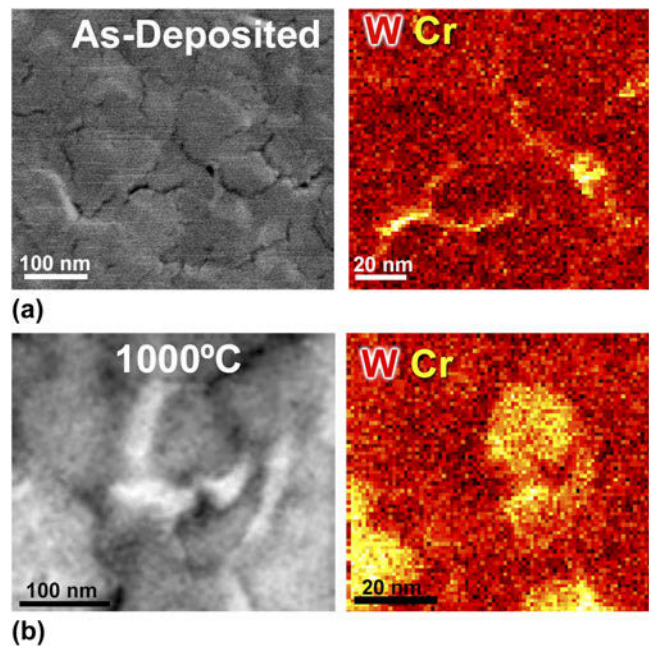


FIG. 11. HAADF images and EELS maps for W-15 at.% Cr film in the (a) as-deposited and (b) 1000 °C annealed conditions. The EELS maps were produced from the entire HAADF images. The as-deposited films exhibited subtle grain boundary segregation whereas Cr-rich regions were detected upon annealing.

Solute distributions in the sputter-deposited films were consistent with the aforementioned results on nanocrystalline tungsten alloys of nominally identical composition albeit synthesized through high-energy ball milling.<sup>43,44</sup> Compositional inhomogeneities exhibited spatial distributions commensurate with characteristic microstructural length scales, indicating the presence of grain boundary segregation as well as solute-rich grains particularly in the W-Cr system. Similar solute dependent grain character distributions have been observed in the phase separating Fe-Cr system and correlated to grain boundary excess volume and energetics in the presence of solute atoms.<sup>66</sup> Solute-rich nanostructured second phases constitutes a unique class of nanocrystalline metals referred to as nanoduplex alloys. Relative to “classical” nanocrystalline alloys stabilized through grain boundary segregation, nanoduplex alloys evolve to a different equilibrium state containing multiple nanostructured phases governed by configurational entropy contributions, and are thus referred to as entropically stabilized alloys.<sup>67</sup> In these systems, less solute is available to segregate to the grain boundaries due to the presence of a solute-rich second phase, and it consequently becomes more difficult to effectively stabilize the nanocrystalline grains against thermal coarsening. This was manifested in the sputter-deposited W-Cr films as enhanced grain growth relative to the W-Ti system where solute-rich grains were absent in the EELS mapping. The reduced thermal stability of the sputter-deposited W-Cr films relative to

W–Ti can therefore be attributed to a shift in the grain boundary segregation state in the presence of a solute-rich second phase, which underscores the role of grain boundary chemistry in solute-stabilized nanocrystalline alloys.

## V. CONCLUSIONS

Microstructural evolution in nanocrystalline tungsten thin films composed primarily of the metastable  $\beta$ -phase was explored through in situ TEM annealing experiments. At temperatures below 550 °C, grain growth transpired through a discontinuous process in turn producing a bimodal grain size distribution containing large nanograins dispersed in the initial small grained nanocrystalline matrix. Abnormal grain growth was coupled to an allotropic phase transformation of metastable  $\beta$  to BCC  $\alpha$ -tungsten, which aligned with previous observations of grain growth in nanocrystalline metals with competing microstructural and phase instabilities. The convergence to a unimodal nanocrystalline structure at 650 °C signaled a transition to continuous, curvature-driven grain growth that was accompanied by complete transformation of the films to BCC  $\alpha$ -tungsten. The addition of alloying elements Ti and Cr eliminated the formation of the metastable  $\beta$ -phase and in turn, stabilized the  $\alpha$ -phase in the as-deposited tungsten alloy films. Both alloys exhibited significantly enhanced thermal stability relative to their unalloyed counterpart up to 1000 °C, and the addition of alloying elements eliminated abnormal grain growth with microstructural evolution instead transpiring through a continuous growth process. Compositional inhomogeneities exhibited spatial distributions that were commensurate with characteristic microstructural length scales, indicating the presence of grain boundary segregation. Solute-rich grains were also present in the W–Cr films and their reduced thermal stability relative to W–Ti was attributed to a shift in the grain boundary segregation state due to the emergence of a solute-rich second phase, thus underscoring the role of grain boundary chemistry in the design of solute-stabilized nanocrystalline alloys.

## ACKNOWLEDGMENTS

Support for this work was provided for OKD and JRT by the National Science Foundation through Grant DMR-1410941 with additional support from the Stony Brook University-Brookhaven National Lab Seed Grant Program. TK and GBT acknowledge support from the Army Research Office through Grant W911NF1310436 and KH from the Materials Science and Engineering Division of the Department of Energy Office of Basic Energy Sciences. The authors gratefully acknowledge Dr. Lihua Zhang of Brookhaven National Laboratory for assistance

with the STEM-EELS measurements and Dr. Brittany Muntifer of Sandia National Laboratories for her guidance on the PED analysis. The authors would also like to thank Dr. Fadi Abdeljawad of Sandia National Laboratories for his valuable insights and feedback. TEM was conducted using resources of the Center for Functional Nanomaterials, Brookhaven National Laboratory, which is supported by the U.S. Department of Energy, Office of Basic Energy Sciences under Contract No. DE-SC0012704. Sandia National Laboratories is a multi-mission laboratory managed and operated by National Technology and Engineering Solutions of Sandia, LLC., a wholly owned subsidiary of Honeywell International, Inc., for the U.S. Department of Energy's National Nuclear Security Administration under contract DE-NA-0003525.

## REFERENCES

1. I.J. Beyerlein, A. Caro, M.J. Demkowicz, N.A. Mara, A. Misra, and B.P. Uberuaga: Radiation damage tolerant nanomaterials. *Mater. Today* **16**, 443 (2013).
2. B.E. Schuster, J.P. Ligda, Z.L. Pan, and Q. Wei: Nanocrystalline refractory metals for extreme condition applications. *JOM* **63**, 27 (2011).
3. S.J. Zinkle and L.L. Snead: Designing radiation resistance in materials for fusion energy. *Annu. Rev. Mater. Res.* **44**, 241 (2014).
4. S. Wurster, N. Baluc, M. Battabyal, T. Crosby, J. Du, C. García-Rosales, A. Hasegawa, A. Hoffmann, A. Kimura, H. Kurishita, R.J. Kurtz, H. Li, S. Noh, J. Reiser, J. Riesch, M. Rieth, W. Setyawan, M. Walter, J.H. You, and R. Pippan: Recent progress in R&D on tungsten alloys for divertor structural and plasma facing materials. *J. Nucl. Mater.* **442**, S181 (2013).
5. T. Hao, Z.Q. Fan, T. Zhang, G.N. Luo, X.P. Wang, C.S. Liu, and Q.F. Fang: Strength and ductility improvement of ultrafine-grained tungsten produced by equal-channel angular pressing. *J. Nucl. Mater.* **455**, 595 (2014).
6. Q. Wei, T. Jiao, K.T. Ramesh, E. Ma, L.J. Kecskes, L. Magness, R. Dowding, V.U. Kazykhanov, and R.Z. Valiev: Mechanical behavior and dynamic failure of high-strength ultrafine grained tungsten under uniaxial compression. *Acta Mater.* **54**, 77 (2006).
7. S. Wurster and R. Pippan: Nanostructured metals under irradiation. *Scr. Mater.* **60**, 1083 (2009).
8. O. El-Atwani, J.A. Hinks, G. Greaves, S. Gonderman, T. Qiu, M. Efe, and J.P. Allain: *In situ* TEM observation of the response of ultrafine- and nanocrystalline-grained tungsten to extreme irradiation environments. *Sci. Rep.* **4** (2014).
9. C. Suryanarayana and C.C. Koch: Nanocrystalline materials: Current research and future directions. *Hyperfine Interact.* **130**, 5 (2000).
10. T. Chookajorn, H.A. Murdoch, and C.A. Schuh: Design of stable nanocrystalline alloys. *Science* **337**, 951 (2012).
11. J. Weissmuller: Alloy effects in nanostructures. *Nanostruct. Mater.* **3**, 261 (1993).
12. T.R. Malow and C.C. Koch: Grain growth of nanocrystalline materials—A review. In *Synthesis and Processing of Nanocrystalline Powder: Proceedings of a Symposium Cosponsored by the Materials Design and Manufacturing Division (MDMD)*, D.L. Bourrell, ed. (Minerals, Metals & Materials Society, Warrendale, Pennsylvania, 1996), pp. 33–44.

13. M. Ames, J. Markmann, R. Karos, A. Michels, A. Tschope, and R. Birringer: Unraveling the nature of room temperature grain growth in nanocrystalline materials. *Acta Mater.* **56**, 4255 (2008).
14. G. Hibbard, J.L. McCrea, G. Palumbo, K.T. Aust, and U. Erb: An initial analysis of mechanisms leading to late stage abnormal grain growth in nanocrystalline Ni. *Scr. Mater.* **47**, 83 (2002).
15. G. Hibbard, K.T. Aust, G. Palumbo, and U. Erb: Thermal stability of electrodeposited nanocrystalline cobalt. *Scr. Mater.* **44**, 513 (2001).
16. G. Riotino, C. Antonione, L. Battezzati, and F. Marino: Kinetics of abnormal grain growth in pure iron. *J. Mater. Sci.* **14**, 86 (1979).
17. S. Simoes, R. Calinas, M.T. Vieira, M.F. Vieira, and P.J. Ferreira: *In situ* TEM study of grain growth in nanocrystalline copper thin films. *Nanotechnology* **21** (2010).
18. R. Dannenberg, E.A. Stach, J.R. Groza, and B.J. Dresser: *In situ* TEM observations of abnormal grain growth, coarsening, and substrate de-wetting in nanocrystalline Ag thin films. *Thin Solid Films* **370**, 54 (2000).
19. J.E. Burke and D. Turnbull: Recrystallization and grain growth. *Prog. Met. Phys.* **3**, 220 (1952).
20. H. Natter, M. Schmelzer, M.S. Löffler, C.E. Krill, A. Fitch, and R. Hempelmann: Grain-growth kinetics of nanocrystalline iron studied *in situ* by synchrotron real-time X-ray diffraction. *J. Phys. Chem. B* **104**, 2467 (2000).
21. J.G. Brons and G.B. Thompson: A comparison of grain boundary evolution during grain growth in fcc metals. *Acta Mater.* **61**, 3936 (2013).
22. V.Y. Gertsman and R. Birringer: On the room temperature grain growth in nanocrystalline copper. *Scr. Metall. Mater.* **30**, 577 (1994).
23. J. Kacher, I.M. Robertson, M. Nowell, J. Knapp, and K. Hattar: Study of rapid grain boundary migration in a nanocrystalline Ni thin film. *Mater. Sci. Eng., A* **528**, 1628 (2011).
24. H. Paul and C.E. Krill: Anomalously linear grain growth in nanocrystalline Fe. *Scr. Mater.* **65**, 5 (2011).
25. J.M. Dake and C.E. Krill, III: Sudden loss of thermal stability in Fe-based nanocrystalline alloys. *Scr. Mater.* **66**, 390 (2012).
26. F. Xiao, W. Cheng, and X.J. Jin: Phase stability in pulse electrodeposited nanograined Co and Fe–Ni. *Scr. Mater.* **62**, 496 (2010).
27. G.D. Hibbard, K.T. Aust, and U. Erb: Thermal stability of electrodeposited nanocrystalline Ni–Co alloys. *Mater. Sci. Eng., A* **433**, 195 (2006).
28. U. Klement and M. Da Silva: Thermal stability of electrodeposited nanocrystalline Ni- and Co-based materials. *J. Iron Steel Res. Int.* **14**, 173 (2007).
29. S.G. Kim and Y.B. Park: Grain boundary segregation, solute drag and abnormal grain growth. *Acta Mater.* **56**, 3739 (2008).
30. R.K. Koju, K.A. Darling, L.J. Kecskes, and Y. Mishin: Zener pinning of grain boundaries and structural stability of immiscible alloys. *JOM* **68**, 1596 (2016).
31. C.V. Thompson: Grain growth in thin films. *Annu. Rev. Mater. Sci.* **20**, 24 (1990).
32. E.A. Holm, M.A. Miodownik, and A.D. Rollett: On abnormal subgrain growth and the origin of recrystallization nuclei. *Acta Mater.* **51**, 2701 (2003).
33. A.L. Garcia, V. Tikare, and E.A. Holm: Three-dimensional simulation of grain growth in a thermal gradient with non-uniform grain boundary mobility. *Scr. Mater.* **59**, 661 (2008).
34. F. Abdeljawad, D.L. Medlin, J.A. Zimmerman, K. Hattar, and S.M. Foiles: A diffuse interface model of grain boundary faceting. *J. Appl. Phys.* **119**, 235306 (2016).
35. S.B. Lee, N.M. Hwang, D.Y. Yoon, and M.F. Henry: Grain boundary faceting and abnormal grain growth in nickel. *Metall. Mater. Trans. A* **31**, 985 (2000).
36. H.J. Frost, C.V. Thompson, and D.T. Walton: Simulation of thin film grain structures—II. Abnormal grain growth. *Acta Metall. Mater.* **40**, 779 (1992).
37. K.A. Darling, A.J. Roberts, Y. Mishin, S.N. Mathaudhu, and L.J. Kecskes: Grain size stabilization of nanocrystalline copper at high temperatures by alloying with tantalum. *J. Alloys Compd.* **573**, 142 (2013).
38. F. Abdeljawad, P. Lu, N. Argibay, B.G. Clark, B.L. Boyce, and S.M. Foiles: Grain boundary segregation in immiscible nanocrystalline alloys. *Acta Mater.* **126**, 528 (2017).
39. J.R. Trelewicz and C.A. Schuh: Grain boundary segregation and thermodynamically stable binary nanocrystalline alloys. *Phys. Rev. B* **79** (2009).
40. F. Liu and R. Kirchheim: Nano-scale grain growth inhibited by reducing grain boundary energy through solute segregation. *J. Cryst. Growth* **264**, 385 (2004).
41. H.A. Murdoch and C.A. Schuh: Estimation of grain boundary segregation enthalpy and its role in stable nanocrystalline alloy design. *J. Mater. Res.* **28**, 2154 (2013).
42. B.G. Clark, K. Hattar, M.T. Marshall, T. Chookajorn, B.L. Boyce, and C.A. Schuh: Thermal stability comparison of nanocrystalline Fe-based binary alloy pairs. *JOM* **68**, 1625 (2016).
43. T. Chookajorn and C.A. Schuh: Nanoscale segregation behavior and high-temperature stability of nanocrystalline W–20 at.% Ti. *Acta Mater.* **73**, 128 (2014).
44. T. Chookajorn, M. Park, and C.A. Schuh: Duplex nanocrystalline alloys: Entropic nanostructure stabilization and a case study on W–Cr. *J. Mater. Res.* **30**, 151 (2015).
45. M.N. Polyakov, T. Chookajorn, M. Mecklenburg, C.A. Schuh, and A.M. Hodge: Sputtered Hf–Ti nanostructures: A segregation and high-temperature stability study. *Acta Mater.* **108**, 8 (2016).
46. S. Dey, C-H. Chang, M. Gong, F. Liu, and R.H.R. Castro: Grain growth resistant nanocrystalline zirconia by targeting zero grain boundary energies. *J. Mater. Res.* **30**, 2991 (2015).
47. Y. Sasanuma, U. Mamoru, K. Okada, K. Yamamoto, Y. Kitano, and A. Ishitani: Characterization of long-periodic layered structures by X-ray diffraction IV: Small angle X-ray diffraction from a superlattice with non-ideal interfaces. *Thin Solid Films* **203**, 113 (1991).
48. A.J. Detor and C.A. Schuh: Microstructural evolution during the heat treatment of nanocrystalline alloys. *J. Mater. Res.* **22**, 3233 (2007).
49. J. Edington: *Practical Electron Microscopy in Materials Science* (Van Nostrand Reinhold Company, New York, New York, 1976).
50. G.P. Williams: Electron binding energies. In *X-ray Data Booklet* 3rd ed., A.C. Thompson, ed. (Center for X-Ray Optics and Advance Light Source, Lawrence Berkeley National Laboratory, Berkeley, California, 2009).
51. R.F. Egerton: Electron energy-loss spectroscopy in the TEM. *Rep. Prog. Phys.* **72**, 016502 (2009).
52. M.J. Okeefe and J.T. Grant: Phase transformation of sputter deposited tungsten thin films with A-15 structure. *J. Appl. Phys.* **79**, 9134 (1996).
53. F.T.N. Vullers and R. Spolenak: Alpha- vs. beta-W nanocrystalline thin films: A comprehensive study of sputter parameters and resulting materials' properties. *Thin Solid Films* **577**, 26 (2015).
54. G.D. Hibbard, G. Palumbo, K.T. Aust, and U. Erb: Nanoscale combined reactions: Non-equilibrium alpha-Co formation in nanocrystalline epsilon-Co by abnormal grain growth. *Philos. Mag.* **86**, 125 (2006).
55. L.N. Brewer, D.M. Follstaedt, K. Hattar, J.A. Knapp, M.A. Rodriguez, and I.M. Robertson: Competitive abnormal grain growth between allotropic phases in nanocrystalline nickel. *Adv. Mater.* **22**, 1161 (2010).

56. P. Choi, M. da Silva, U. Klement, T. Al-Kassab, and R. Kirchheim: Thermal stability of electrodeposited nanocrystalline Co–1.1 at.% P. *Acta Mater.* **53**, 4473 (2005).
57. J. Kacher, K. Hattar, and I.M. Robertson: Initial texture effects on the thermal stability and grain growth behavior of nanocrystalline Ni thin films. *Mater. Sci. Eng., A* **675**, 110 (2016).
58. J.G. Brons and G.B. Thompson: Orientation mapping via precession-enhanced electron diffraction and its applications in materials science. *JOM* **66**, 165 (2014).
59. W.W. Mullins: Theory of thermal grooving. *J. Appl. Phys.* **28**, 333 (1957).
60. P. Sachenko, J.H. Schneibel, and W. Zhang: Effect of faceting on the thermal grain-boundary grooving of tungsten. *Philos. Mag. A* **82**, 815 (2002).
61. E.A. Holm, G.N. Hassold, and M.A. Miodownik: On misorientation distribution evolution during anisotropic grain growth. *Acta Mater.* **49**, 2981 (2001).
62. D.L. Olmsted, S.M. Foiles, and E.A. Holm: Survey of computed grain boundary properties in face-centered cubic metals: I. Grain boundary energy. *Acta Mater.* **57**, 3694 (2009).
63. J. Gruber, H.M. Miller, T.D. Hoffmann, G.S. Rohrer, and A.D. Rollett: Misorientation texture development during grain growth. Part I: Simulation and experiment. *Acta Mater.* **57**, 6102 (2009).
64. S.J. Dillon and G.S. Rohrer: Mechanism for the development of anisotropic grain boundary character distributions during normal grain growth. *Acta Mater.* **57**, 1 (2009).
65. J.G. Brons and G.B. Thompson: Abnormalities associated with grain growth in solid solution Cu(Ni) thin films. *Thin Solid Films* **558**, 170 (2014).
66. X.Y. Zhou, X.X. Yu, T. Kaub, R.L. Martens, and G.B. Thompson: Grain boundary specific segregation in nanocrystalline Fe(Cr). *Sci. Rep.* **6** (2016).
67. W. Xing, A.R. Kalidindi, and C.A. Schuh: Preferred nanocrystalline configurations in ternary and multicomponent alloys. *Scr. Mater.* **127**, 136 (2017).